Magnetic Resonance Imaging 115 (2025) 110247

Contents lists available at ScienceDirect

Magnetic Resonance Imaging

journal homepage: www.elsevier.com/locate/mri

Deep learning corrects artifacts in RASER MRI profiles

Moritz Becker, Filip Arvidsson, Jonas Bertilson, Elene Aslanikashvili, Jan G. Korvink, Mazin Jouda, Sören Lehmkuhl *

Institute of Microstructure Technology, Karlsruhe Institute of Technology, Hermann-von-Helmholtz-Platz 1, Eggenstein-Leopoldshafen 76344, Germany

ARTICLE INFO

Keywords:
MRI
RASER
Hyperpolarization
Deep learning
Artifact removal

ABSTRACT

A newly developed magnetic resonance imaging (MRI) approach is based on "Radiowave amplification by the stimulated emission of radiation" (RASER). RASER MRI potentially allows for higher resolution, is inherently background-free, and does not require radio-frequency excitation. However, RASER MRI can be "nearly unusable" as heavy distortions from nonlinear effects can occur. In this work, we show that deep learning (DL) reduces such artifacts in RASER images. We trained a two-step DL pipeline on purely synthetic data, which was generated based on a previously published, theoretical model for RASER MRI. A convolutional neural network was trained on 630′000 1D RASER projections, and a U-net on 2D random images. The DL pipeline generalizes well when applied from synthetic to experimental RASER MRI data.

1. Introduction

Magnetic resonance imaging (MRI) is a key technology that allows for destruction-free studies of living and inanimate samples. MRI is embedded within the modern healthcare system, and enables the diagnosis of diverse diseases. Despite its broad applicability, there remains an ongoing quest for the development of personalized medicine, imaging function, in addition to structure. Over the last decade, clinical trials with molecular contrast agents have demonstrated their applicability to many medical questions. The most prominent molecular contrast agent is 13C-labeled pyruvate, which can be used to track the metabolism in various types of cancer [1–3]. To achieve the required sensitivity needed for imaging, these agents are hyperpolarized with different techniques such as dynamic nuclear polarization (DNP) [4,5], spin exchange optical pumping (SEOP) [6,7], and parahydrogen-induced polarization (PHIP) [8,9]. Despite the spin polarizations (> 10%) that are achieved, even more sensitivity is desirable due to the low concentration of relevant metabolites. This motivates the search for novel, complementary detection schemes that increase sensitivity even more.

In 2022, it was demonstrated that the RASER concept could be extended to MRI, enabling the use of this new detection scheme. [10] (RASER = Radiowave amplification by the stimulated emission of radiation). The RASER, mimicking the LASER, uses stimulated radio-frequency emission, instead of an external perturbation source to excite quantum particles. To obtain the RASER effect, a population inversion (i.e. negative polarization) is required. Fortunately, the hyperpolarization techniques, already used for molecular contrast agents, have all been shown recently to generate high polarization levels and fuel RASERs on different nuclei, including ^{1}H [11–13], ^{3}He [14], ^{13}C [15], ^{17}O [16], ^{7}Li and ^{31}P [17], or ^{27}AL [18]. We generated a large negative polarization difference with the parahydrogen-based SABRE approach [19] (SABRE = Signal Amplification By Reversible Exchange; Fig. 1a, left). The detection scheme for the RASER approach in MRI is quite straightforward. After the nuclear spins are spontaneously self-excited, the radio-frequency response is encoded using magnetic field gradients during acquisition, and processed into a spectrum or an image by known MR techniques, or projection reconstruction analogues to computed tomography (CT). RASER signals are inherently background-free [20], do not require external RF excitation [21] and hence can lead to highly-resolved spectra [21,22], or images [10] that are resolved at a higher level than previously thought possible. However, the advantages come at a cost. The nonlinear interactions in a RASER-active system introduce new types of artifacts [23–25].

An example of such artifacts is shown in Fig. 1a (top), for a standard NMR tube with 4.1 mm inner diameter containing the analyte. It is still an open question whether it is possible to remove these artifacts. Considering they arise from highly non-linear effects, an analytical solution may not be tangible. Therefore, we chose a data-driven approach to see whether it is possible to remove these artifacts. Throughout this work, we demonstrate that it is possible to at least reduce the artifacts by

* Corresponding author.
E-mail address: soeren.lehmkuhl@kit.edu (S. Lehmkuhl).

https://doi.org/10.1016/j.mri.2024.110247
Received 8 July 2024; Received in revised form 23 September 2024; Accepted 29 September 2024
Available online 24 October 2024

applying deep learning (DL), where the neural network is trained purely on simulation-based data. Many studies show how DL applied to CT or MRI can improve image quality by reducing noise or removing artifacts [26–29], e.g., caused by hardware imperfections. However, to the best of our knowledge, no suitable other approach exists for correcting RASER MRI images. DL models, as a subgroup of artificial intelligence (AI), have demonstrated great success over various domains by end-to-end learning, i.e., an algorithm learns, given only the input and the target, to automatically detect correlations. One could argue that DL confirms the likelihood that the target lies within the reachable space of the input. DL models are implemented as stacked layers of artificial neurons, where a model learns by updating its neuronal weights through backpropagation and gradient descent, to minimize a given loss function on the training set. A more detailed description of DL is given in LeCun et al. [30]. For our DL approach, we considered that the simplest approach would be to "correct" the individual projections, rather than correcting the image as a whole. This reduced our problem to a single spatial dimension, commensurate with a Radon transfer, and saved computational power. The 2D image could then be obtained by the Radon transform of an individual projection, and the image as a whole could be cleaned up in a consecutive AI-driven step.

2. Generating a dataset, suitable to train the neural net

Deep learning typically requires large amounts of (labeled) training data. However, RASER MRI is a very new technique, so that few prior images exist. This challenge is further complicated by the fact that hyperpolarized MRI is not yet very well automated. Thus, measuring a dataset with tens of thousands of images in a short amount of time is simply impossible. As an alternative, we used the RASER equations [10,31] to simulate an entire set of training data for our neural network. A common issue of DL models trained in simulation is the so-called reality gap, which usually prevents any model from successfully generalizing to the real world if trained in another domain. To ensure that our dataset can be applied effectively across different RASER MRI environments, settings, and imaging subjects, we used domain randomization [32]. This approach involves creating data with arbitrary variations within an experimentally realizable parameter space. Specifically, by exposing our model to images with random noise, artifacts, and variability in image quality, we make it more robust and capable of generalizing to real-world data. Suppose our model is trained with images from a vast amount of different domains. Thus, to our model, reality would appear as another arbitrary domain. Following this idea, we generated a large set of random images as a basis for the RASER signal simulations (see Fig. 2). Details of the random image generator are given in the supplementary section. For each batch of images, we simulated the RASER signals that would be yielded from N different image projections. When Fourier transformed, these signals gave us the distorted RASER projections, which constituted a dataset together with their "labeled" references. For our training dataset, we opted for $N = 30$ projections (angles) with a limit of 64 pixels along each projection direction. This decision was primarily motivated by the proof-of-concept style of our study, and the computational complexity when scaling to more pixels (see SI). Within this selected parameter space, however, we chose vast augmentation to artificially inflate the amount of data and ensure model generalization.

The RASER simulation is governed by a set of parameters (see Fig. 2). The most important experimental parameters can be summarized by defining a parameter ε as a measure of how far the system is operated above the RASER threshold

$$\varepsilon = d_0/d_{th} \tag{1}$$

with the RASER threshold

$$d_{th} = 4 \cdot V_S / \left(\mu_0 \cdot \hbar \cdot Q \cdot \gamma^2 \cdot T_2^*\right), \tag{2}$$

where $\hbar$ is the reduced Planck constant, and μ_0 is the vacuum permeability. The number of spins that are population inverted at the begin-

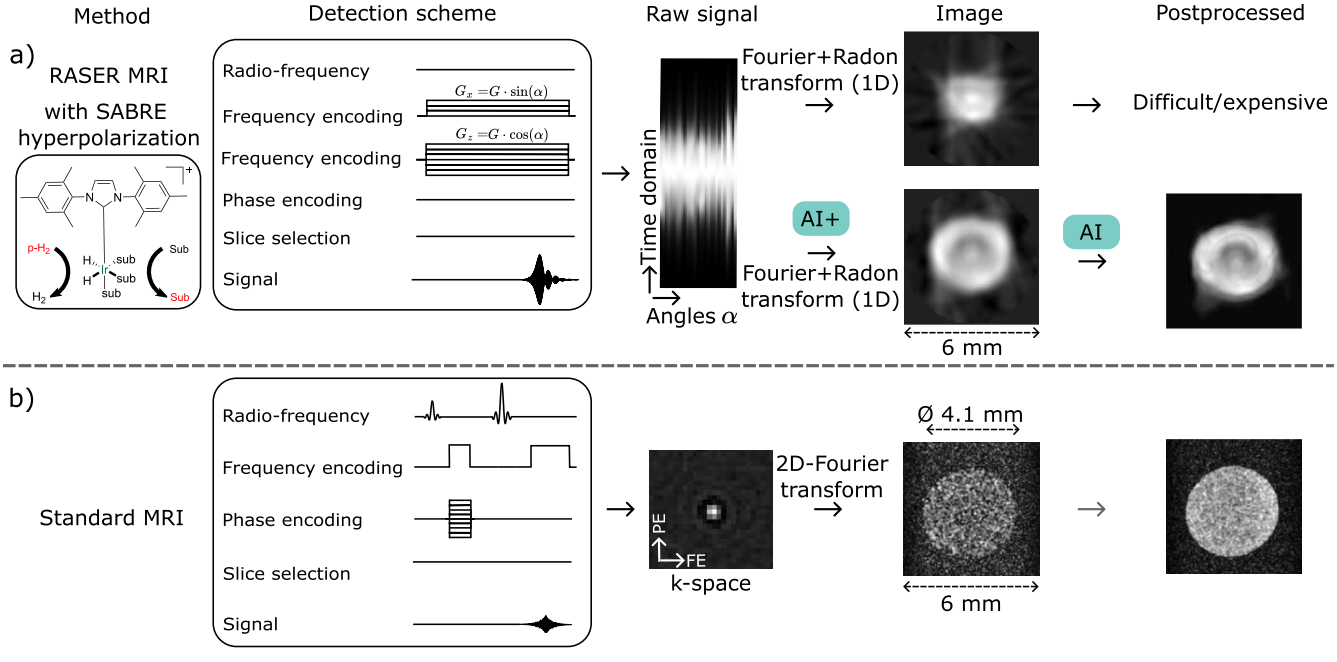

Fig. 1. Deep learning corrects artifacts in RASER MRI profiles. a) Detection scheme of a RASER image: First, a population inversion is generated using SABRE hyperpolarization of pyrazine at 6.5 mT in a 5 mm NMR tube. The tube is then transferred into a 1.5 T benchtop NMR magnet, where one projection is recorded at a gradient of 0.26G/m. This hyperpolarization and detection scheme is repeated for each angle and the resulting projections are collected in a sinogram. A distorted image is obtained after Fourier and Radon transform. The individual projections of the sinogram can be corrected using artificial intelligence (AI). Further, AI can help to enhance the full 2D image (field-of-view (FOV) = 7.4 mm × 7.4 mm with 67 × 67 pixels). b) Detection scheme of an MRI reference image: A spin echo image of a 10/90 % H_2O/D_2O mixture is measured in a 5 mm NMR tube (inner diameter = 4.1 mm, FOV = 7.4 mm × 7.4 mm with 128 × 128 pixels, gradient = 79 G/m). The obtained image can be enhanced by traditional or DL-based post-processing approaches.

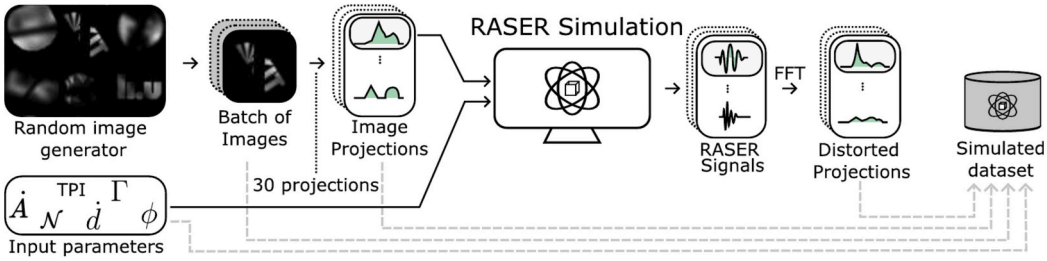

Fig. 2. Generating a RASER MRI training set from simulation data. A batch of images is obtained using a random image generator (details see SI). 30 projections of each image, taken along different angles, were fed into the simulation along with experimental parameters, which were varied widely (details see text) to ensure augmentation. The simulated RASER signals for each projection exhibited nonlinear effects, which depended on the different input parameters of the simulation. A Fourier transform of the signals gave the distorted projections, which could be compared to the targets, resulting in a labeled dataset.

ning of the experiments, d_0, is a measure of the total population inversion (TPI). It is therefore determined by the spin density and its negative polarization. For our test molecule pyrazine, with four magnetically equivalent protons, this equals four times the negative molar polarization, a metric introduced in the context of metabolic imaging with fumarate [33]. By varying ε through our simulations, we not only accounted for changes in concentrations, and the polarization difference between experiments, but also for other effects such as polarization losses before the onset of the experiment, e.g., due to relaxation in a less efficient resonator (characterized by Q), or a less homogeneous magnetic field B_0 (characterized by T_2^*). Additionally, the nonlinear effect strongly depended on how far the system was above the RASER threshold [10,23,25].

For our augmentation, we chose $\varepsilon = 3{\cdot}10^{16}{\cdot}\mathcal{N}(1,\sigma)$ with different noise variances σ for both different signals of projections within one image and among images. In addition, we chose to assign the starting signal amplitude A and phase φ to a random value within the scope of typical experimental noise, while φ experienced uniform and A normal noise, respectively. Finally, we also considered variations in the polarization pumping rate Γ. Polarization pumping can for example happen through polarized molecules entering the sensitive volume of the NMR detection (e.g. by diffusion). In low-field experiments, additional SABRE pumping still occurs after the bubbling or shaking of the sample has been halted. This can be either through dissolved parahydrogen or by additional parahydrogen dissolving when a capillary is still in the solution. We included simulations with a decaying pumping rate Γ representing a case similar to the parahydrogen-pumping needles as in Lehmkuhl et al. [10]. The pumping terms are added in two random positions between positions 24 and 42 of each projection, avoiding pumping close to the boundaries, which can cause ripple effects in the signal.

Each individual image, together with its 30 projections, simulation parameters, and distorted spectra, were stored as one sample of the simulated dataset (see Fig. 2). Formally, we created a static dataset $\mathscr{D} = \{(\mathbf{x},\mathbf{y})_i\}_{i=1}^{|\mathscr{D}|}$, where $\mathbf{x}$ is the input, and $\mathscr{T}_i = \left\{\left(k_j, p_j\right)_i\right\}_{j=1}^{N}$ are subsets for every $\mathbf{x}$ with N projections/angles. In detail, let $\mathbf{x} \in \mathbb{R}^{44\times44}$ be a random generated image, and $p_1 \ldots p_j \in \mathbb{R}^{1\times67}$ be projections thereof, with j being the number of projections/angles. Each projection underwent a RASER simulation with different parameters (TPI, pumping, …), yielding a RASER signal $r_j = R_\alpha\left(p_j\right) \in \mathbb{R}^{1\times4096}$. The distorted spectra $k_j \in \mathbb{R}^{1\times200}$ were obtained by Fourier transform (FFT) of r_j. By Radon transform (RT) of the absolute of spectra k_j, we obtained a RASER image $\mathbf{z} = \mathrm{RT}(k_1, \ldots, k_N)$ with artifacts.

In total, we simulated 10.000 images without pumping, and 10.000 images with pumping, as well as 1.000 images with high fluctuations in the polarization level between the projections of one experiment. In total, this gave 21.000 images with over 630 k pairs of distorted and target spectra, available for download from Becker et al. [34]. We also generated 100 additional images as a hold-out test set for performance evaluation.

3. Deep learning training pipeline based on a RASER simulation

After generating the simulated data, we trained our DL models on these to correct for RASER MRI artifacts. Our AI-driven approach for correcting RASER MRI images included two different AI models applied consecutively (see Fig. 3): The first model used a convolutional neural network (CNN) to correct the one-dimensional projections that made up the sinogram, one at a time. This model mainly aimed at correcting the nonlinear artifacts generated by the interaction between the spins during the RASER. A Radon transform of the corrected sinogram yielded an AI-corrected image. This image could be further optimized using an additional model. The second model was based on a U-Net architecture [35] and took the whole image into account, not only individual projections. It also helped to denoise the image and increase contrast, such that the predicted image matched the target image before the RASER simulation.

In detail, both phases were trained with our simulated dataset $\mathscr{D} = \{\mathbf{x}_i\}_{i=1}^{|\mathscr{D}|}$, the first model on 1D distorted projections, and the second on 2D RASER images.

Formally, the first phase used a 1D model $F_{\theta_A}^{A}\left(k_j\right)$, where F^A is a CNN with parameters θ_A, that is supposed to correct each distorted spectra k_j to its original projection counterpart $\widehat{p}_j = F_{\theta_A}^{A}\left(k_j\right)$. Ideally, $\widehat{y} = \mathrm{RT}(\widehat{p}_1, \ldots, \widehat{p}_N)$ of all corrected projections should match the random image $\mathbf{x}$, and be of better quality/resolution than the RASER image $\mathbf{z}$. The CNN model is trained in a supervised manner using subset $\mathscr{T}$ to minimize the mean squared error (MSE) loss $\mathscr{L}_1$ between the predictions $\widehat{p}$ and p.

The second correction phase incorporated an additional model $\widehat{\mathbf{x}} = F_{\theta_B}^{B}(\widehat{\mathbf{y}})$, where F^B was an encoder-decoder architecture based on U-Net [35] with parameters θ_B, to denoise the 1D-corrected image $\widehat{\mathbf{y}}$ to $\mathbf{x} = \widehat{\mathbf{x}}$. The U-Net model was trained to minimize the mean absolute error (MAE) loss $\mathscr{L}_2$ between $\mathbf{x}$ and $\widehat{\mathbf{x}}$.

Details of the DL training and the neural network architectures are given in the supplementary.

With these two DL models trained on our simulated RASER image dataset we evaluated the overall performance of our approach, as presented next.

4. Removing artifacts in RASER images with AI

To assess the overall performance, we first tested our approach on a hold-out test set from our random image generator. In a second step, we tested our approach on an out-of-distribution image. Finally, we tested with experimental data. For the prior, we chose the modified Shepp-Logan phantom, a commonly used CT phantom (see Fig. 4 A-D) and for the latter we recorded a RASER image using SABRE hyperpolarization [19] in a 5 mm NMR tube (Fig. 4 *E*-H).

First, we evaluated our AI pipeline on our hold-out test set. In detail, we report the mean squared error (MSE) and structural similarity index

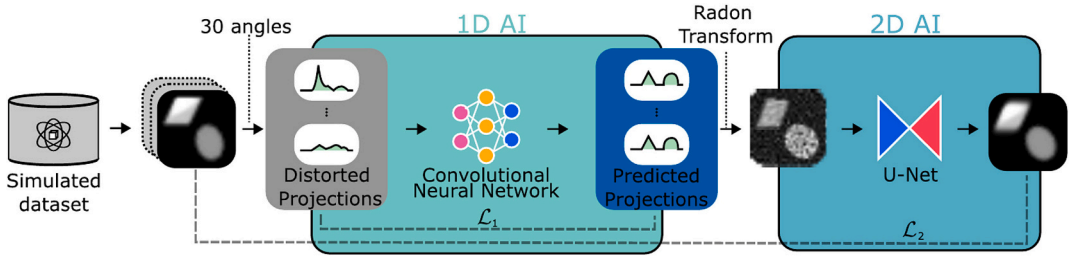

Fig. 3. Two-Stage Deep Learning (DL) pipeline. Random images and corresponding projections from a simulated dataset were fed to our DL models. A convolutional neural network corrected one-dimensional distorted spectra, which were reconstructed with the Radon transform to an image. This image was further enhanced by a U-Net model.

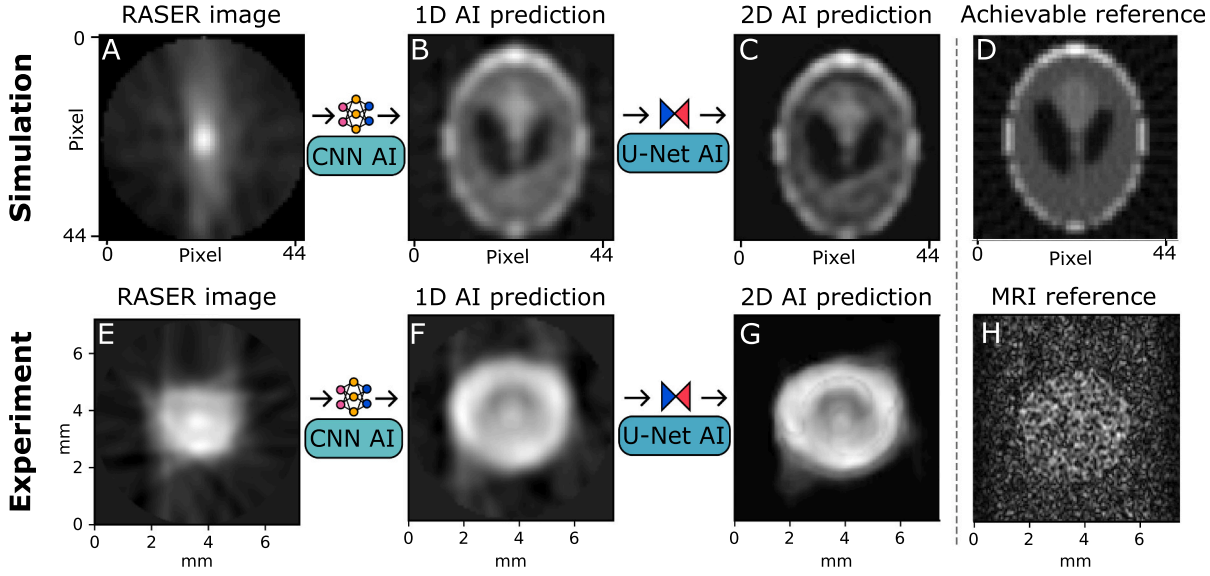

Fig. 4. AI-correction of the Shepp-Logan phantom in simulation (A-D), and an experimental RASER image (*E*-H). The distorted RASER images (A,E) were corrected in a first step with the 1D CNN model (B,F). A second step with a 2D U-Net enhanced image quality further (C,G). The best achievable reference for the simulated Shepp-Logan phantom, reconstructed with Radon transform from only 30 projections, is shown in (D), and reference spin echo image in (H). Experimental images were obtained at 1.5 T with a 60 mmol L^{-1} solution of SABRE-hyperpolarized pyrazine in deuterated methanol, and the FOV for both images is 7.4 mm × 7.4 mm with 128 × 128 pixels for MRI, and 67 × 67 pixels for RASER, respectively.

measure (SSIM) [36], a quality measure based on human perception, to assess the qualitative performance of our networks for artifact removal and/or RASER MRI image reconstruction. For MSE, lower values ($\in \mathbb{R}_{>0}$) are preferred, and for SSIM, higher values ($\in [0,1]$) are desirable.

On the hold-out test set with 100 randomly generated images, the model achieved 0.002 ± 0.002 MSE and 0.906 ± 0.065 SSIM, on average.

For out-of-distribution testing, 30 projections of the simulated Shepp-Logan phantom (D) were taken, which were subject to our RASER simulation. The reassembled image (A) did not show any recognizable features and had clear artifacts. After correcting the 1D projections with our 1D CNN model, and Radon transform of the predicted sinogram, the main features of the phantom were visible (B). Contrast and quality were further enhanced after predictions with our U-Net (C). The model's predictions were quite close to the target (D) and allowed for the inspection of important structures. Quantitatively speaking, the model achieved an MSE of 0.056, and SSIM of 0.275, after AI-driven correction of the 1D signals (B), and an MSE of 0.026, and SSIM of 0.599, after the full correction pipeline, depicted in (C). Note that even with perfect prediction performance of our U-Net model, (C) cannot reach full reconstruction quality of (D) due to losses during filtered back projection from a sinogram with only 30 projections to the image.

The models' generalization is demonstrated with an experimental RASER image using a standard 5 mm glass tube on a 1.5 T benchtop NMR spectrometer(Fig. 4 E-H). The experiments were conducted such that they match the simulation's dimensionalities. The RASER image (E) was measured using SABRE hyperpolarized pyrazine with a molar polarization of -1.2 mmol L^{-1} at a gradient of 26 μTm^{-1}. (more details are provided in the SI). Our SABRE polarization was reproducible to ±5% between each projection, falling below a polarization fluctuation of up to ±20% during the training of our neural network. Due to the low gradient and high molar polarization, the RASER is higher above the threshold than in the previous work. This results in stronger nonlinear artifacts to provide the AI with a reasonable challenge. As a reference, a traditional, (hyperpolarization-free) image is recorded using a spin-echo sequence (H) and at a much higher gradient of 7.9 mTm^{-1}. The RASER image shows severe artifacts, but after AI correction of the image projections, the real geometric dimensions of the glass tube are clearly visible (inner diameter of 4.1 mm in (F)). The image quality could be further improved by 2D image enhancement using AI (G). Nonetheless, the RASER image shows an oval-like shape with approximately 4.1 × 4.5 mm (MRI reference diameter 4.1 mm). This dougnut-like appearance of the image may be caused by the inhomogeneity of the B_1 field, which is stronger at the boundaries of the sample. Note that for these experiments, a reference image without artifacts was not available due to the novelty of RASER MRI, and thus, we could not calculate qualitative metrics. This is expected to change in the future.

5. Discussion & outlook

In this work, we demonstrated that it is possible to reduce artifacts from RASER images, despite strong nonlinear perturbations. Our two-step AI model could correct otherwise unrecognizable images. Due to the limited availability of measured RASER images, the models were solely trained on synthetic data.

The simulations were based on a theoretical model of RASER MRI [10], which accounts well enough for the nonlinear effects arising in a RASER system. This includes the effects of strong radiation damping and coupling between the different RASER active frequencies. Distant dipolar fields, which typically plague such nonlinear systems [11,37,38], only played a minor role in previous parahydrogen RASER experiments [10,21,25]. The simulations themselves were limited to a maximum number of $M = 67$ modes to reduce the computational (and with it, environmental) footprint, as the required simulation time roughly scales cubically with the number of modes M (see supplementary Fig. D.6). This came at a cost because current AI cannot yet extrapolate to predict larger images correctly, due to the inherent properties of nonlinear interactions (they scale nonlinearly with distance).

Despite the current limitations, cleaning up RASER images using AI is not only the first, but also a very promising technique. The corrected images are nearly independent of the nonlinear effects if there is enough signal.

Code availability

The code is available via GitHub at github.com/mobecks/raser-mri-ai. The dataset is publicly available at Becker et al. [34].

CRediT authorship contribution statement

Moritz Becker: Writing – review & editing, Writing – original draft, Visualization, Software, Investigation. **Filip Arvidsson:** Visualization, Software, Investigation. **Jonas Bertilson:** Visualization, Software, Investigation. **Elene Aslanikashvili:** Writing – review & editing, Validation, Investigation. **Jan G. Korvink:** Writing – review & editing, Supervision, Project administration, Funding acquisition. **Mazin Jouda:** Writing – review & editing, Supervision, Project administration, Funding acquisition. **Sören Lehmkuhl:** Writing – review & editing, Writing – original draft, Supervision, Software, Project administration, Funding acquisition, Conceptualization.

Declaration of competing interest

J.G.K. is a shareholder of Voxalytic GmbH. The other authors declare no competing interests.

Acknowledgements

The authors acknowledge partial support from the Deutsche Forschungsgemeinschaft (DFG, German Research Foundation) under contract 389084717, and the CRC HyPERiON 1527/1 under contract 454252029. SL acknowledges support from the DFG for his Emmy Noether group under contract 528402160. We further acknowledge support from the Helmholtz Society's program *Materials Systems Engineering*, in the *Research Area Information*. The authors appreciate financial support by the KIT-Publication Fund. MB thanks Alfredo for fruitful discussions. We thank Craig Eccles from Magritek for his great support and for providing benchtop imaging sequences. We also thank Peng Wang for his constant help with the simulation code. We greatly thank Jakoba Wacker for her help with the experiments.

Appendix A. Random image generator details

Random images for the simulation of RASER signals combined basic shapes and image transformations. We arbitrarily selected 2 to 20 shapes with a random opacity $\in [0, 1]$ from circle (80 %) or polygon shapes with 4–8 vertices. Additionally, Gaussian blur was applied with a 50 % probability, and noise was added with a 30 % probability. Each image was then masked with a circle (56 %), square (24 %), star (5 %), scribble (5 %), KIT logo (5 %), or liu logo (5 %), each scaled randomly between 50 and 100 % of the image's width and with the center location shifted to within $1/4$ of the image size, also rotated and blurred randomly. Finally, a line with random width, random rotation, and 30 % Gaussian blur was added to 80 % of the images.

Appendix B. DL details

B.1. Normalization

All image projections were zero-padded by double the number of points on both sides of the time domain to increase the resolution for the subsequent Fourier transform. Then, the absolute value of the spectrum was cut to a region of interest (ROI) of size 200 centered at the maximum value, then normalized to $[0, 1]$ w.r.t. the TPI value. The regression targets, i.e., the target projections, were normalized to $[0, 1]$.

B.2. Architectures

The neural network used for step 1 was a vanilla convolutional neural network with 3 convolutional (each consisting of convolution, ReLU, dropout, pooling) blocks with kernel size of 8, 64 filters, pooling 2, followed by 5 fully connected layers (each with FC, activation, dropout) with 1024 hidden neurons. The final activation was an exponential linear unit (ELU), and all dropout rates were 0.2. Step 2 was based on a U-net architecture with reduced feature size, from github.com/aladdinpersson/Machine-Learning-Collection. Our final models were carefully selected from a large cohort of candidates, all trained with limited neural architecture search (NAS) and automated hyperparameter optimization (HPO) using raytune [39]. We tested FC and CNN with different hyperparameters for 1D, autoencoders and UNet with varying input-output combinations, including sinogram-image (inspired by Zhang et al. [40]), image-image, and sino-sino for 2D. Further details are also given in Arvidsson and Bertilson [41].

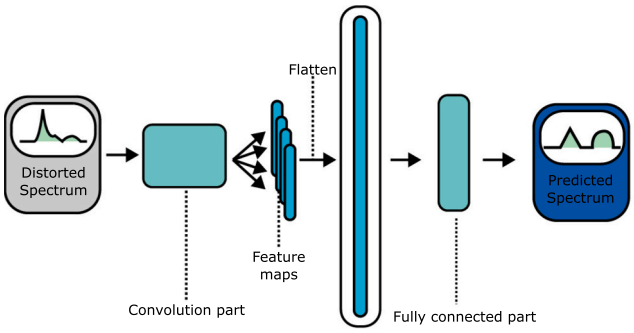

(a) Convolutional neural network for 1D projection correction.

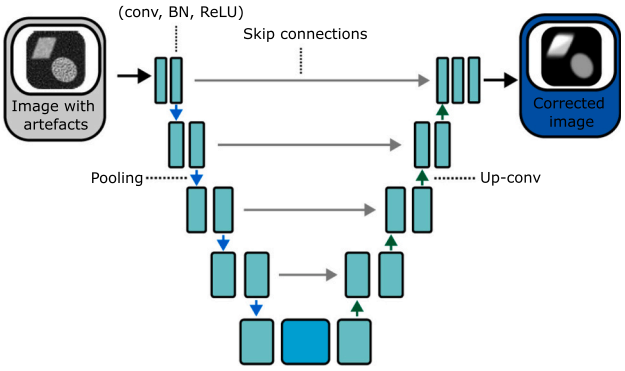

(b) U-net architecture for 2D RASER image enhancement.

Fig. B.5. Neural network architectures.

B.3. Training

We trained our models using the Pytorch framework [42]. The CNN model was trained for 500 epochs, and a batch size of 300 to minimize the MSE loss. The U-Net model was trained for 20 epochs with a batch size of 5 to minimize MAE. Both models used the Adam optimizer [43] with a learning rate of 4.145×10^{-5} and weight decay of 1.012×10^{-6}.

B.4. Hardware requirements

We generated our simulated dataset and performed DL training with an AMD Ryzen 95,950× equipped with 64GB RAM and a graphics processing unit NVIDIA GeForce RTX 3080Ti. The datasets roughly required 99.6GB of disc space. The trained models required approximately 28 MB and 2 MB of disc space for CNN and U-Net, respectively. The simulation time of one image with 67 modes and 30 angles was roughly half a minute (24 s to 43 s) on a Ryzen 95,950× workstation with 64GB of RAM with MATLAB R2023a, giving a total simulation time of more than seven days for our entire dataset.

Appendix C. Experimental setup for experimental measurements

C.1. Synthesis of Ir-IMes catalyst

In a purged Schlenk flask, 1,3-bis(2,4,6-trimetylphenyl)-imidazol-1-ium chloride (341 mg, 1 mmol, 1.00 eq.) and $C_{16}H_{24}Cl_2Ir_2$ (403 mg, 0.6 mmol, 0.6 eq.) were dissolved in dry THF (10 mL) under argon atmosphere. Potassium tert-butoxide (134 mg, 1.2 mmol, 1.2 eq.) was dissolved in dry THF (4 mL), and dropwise added to the reaction flask under vigorous stirring. The mixture was stirred for 30 min, and then methylene chloride (20 mL) was added. The organic phase was washed with distilled water (2 × 19mL), dried over Na_2SO_4, and concentrated under reduced pressure. The resulting residue was purified by flash column chromatography on silica gel using methylene chloride to provide $IrClC_{29}H_{36}N_2$ (0.451 mg, 70.3 %) as a yellow solid.

C.2. SABRE sample preparation

For our SABRE sample, individual stock solutions of the Ir-IMes catalyst and pyrazine were prepared, 6 mmol L^{-1}, and 120 mmol, respectively. All solutions were made with deuterated methanol under inert gas conditions. The deuterated methanol was degassed by three freeze-pump-thaw cycles. 350 µL of each stock solution was transferred into a standard 5 mm NMR tube to result in a 700 µL sample with 3 mmol catalyst and 60 mmol pyrazine concentration.

C.3. Parahydrogen generation

The parahydrogen gas of 98 % fraction used in the SABRE experiments was obtained using a commercial helium compressor at 23 K. The catalyst used in the generator was Iron (III) oxide hydroxide.

C.4. Parahydrogen bubbling experiments

To ensure maximum polarization build-up, parahydrogen gas was bubbled with a thin needle through the sample for 20 s, while being placed in a 6.5 mT magnetic field. This generated a polarization of about −2.0 % on pyrazine (molar polarization of -1.2 mmol L^{-1}). Consecutively, the needle was removed from the tube, and the tube inserted into the spectrometer for detection within two seconds. This manual process is still unreasonable for in-vivo measurements, but can already be automated [44].

C.5. NMR spectroscopy (detection and processing)

After generating the required population inversion with SABRE, the RASER signal is detected in a 60 MHz benchtop spectrometer in the presence of a frequency encoding gradient of 26 μTm^{-1}. A 1D projection is obtained after a Fourier Transform of the signal. By switching the gradient direction between different RASER acquisitions, different projections can be acquired and collected in a sinogram, which can be translated into a 2D image by a Radon transform analogue to computed tomography (CT). ^{1}H NMR spectra were recorded on the Magritek Spinsolve 60 MHz benchtop NMR spectrometer. Without an excitation RF pulse, the receiver signal with 32,768 points was recorded with a dwell time of 500 μs, and a bandwidth of 2 kHz. The NMR spectra were recorded at room temperature in deuterated methanol from Sigma Aldrich.

C.6. MR reference image

The MR reference image in Fig. 4 (H) was recorded using a 10/90 % H_2O/D_2O mixture (molar polarization of 26 μmol L^{-1}). The shim coils generated a gradient of up to 7.9 mTm^{-1}. The image was acquired within 54.2 s without averaging, by only filling 50 % of k-space and using the following parameters: 7.4 mm × 7.4 mm field-of-view (FOV), 400 μs dwell time, 60 ms echo time, 500 ms repetition time, 4 dummy scans, 2.5 kHz bandwidth, 12.3 μs pulse length, 128 points, and a tip angle of 45°.

Appendix D. Supplementary data

Supplementary data to this article can be found online at https://doi.org/10.1016/j.mri.2024.110247.

References

[1] Kurhanewicz J, Vigneron DB, Ardenkjaer-Larsen JH, Bankson JA, Brindle K, Cunningham CH, et al. Hyperpolarized (13)C MRI: path to clinical translation in oncology. Neoplasia 2019;21:1–16. URL, https://www.ncbi.nlm.nih.gov/pubmed/30472500. https://doi.org/10.1016/j.neo.2018.09.006.

[2] Kurhanewicz J, Vigneron DB, Brindle K, Chekmenev EY, Comment A, Cunningham CH, et al. Analysis of cancer metabolism by imaging hyperpolarized nuclei: prospects for translation to clinical research. Neoplasia 2011;13:81–97. URL, https://www.ncbi.nlm.nih.gov/pubmed/21403835. https://doi.org/10.1593/neo.101102.

[3] Nantogma S, de Maissin H, Adelabu I, Abdurraheem A, Nelson C, Chukanov NV, et al. Carbon-13 radiofrequency amplification by stimulated emission of radiation of the hyperpolarized ketone and hemiketal forms of allyl [1-(13)C]pyruvate. ACS Sens 2024;9:770–80. URL, https://www.ncbi.nlm.nih.gov/pubmed/38198709. https://doi.org/10.1021/acssensors.3c02075.

[4] Abraham M, McCausland MAH, Robinson FNH. Dynamic nuclear polarization. Phys Rev Lett 1959;2:449–51. https://doi.org/10.1103/PhysRevLett.2.449.

[5] Barker WA. Dynamic nuclear polarization. Rev Mod Phys 1962;34:173–85. https://doi.org/10.1103/RevModPhys.34.173.

[6] Navon G, Song YQ, Rõõm T, Appelt S, Taylor RE, Pines A. Enhancement of solution NMR and MRI with laser-polarized xenon. Science 1996;271:1848–51. https://doi.org/10.1126/science.271.5257.1848.

[7] Walker TG, Happer W. Spin-exchange optical pumping of noble-gas nuclei. Rev Mod Phys Apr 1997;69:629–42. URL: https://link.aps.org/doi/10.1103/RevModPhys.69.629. https://doi.org/10.1103/RevModPhys.69.629.

[8] Bowers CR, Weitekamp DP. Transformation of symmetrization order to nuclear-spin magnetization by chemical reaction and nuclear magnetic resonance. Phys Rev Lett 1986;57:2645–8. https://doi.org/10.1103/PhysRevLett.57.2645.

[9] Bowers CR, Weitekamp DP. Parahydrogen and synthesis allow dramatically enhanced nuclear alignment. J Am Chem Soc 1987;109:5541–2. https://doi.org/10.1021/ja00252a049.

[10] Lehmkuhl S, Fleischer S, Lohmann L, Rosen MS, Chekmenev EY, Adams A, et al. RASER MRI: magnetic resonance images formed spontaneously exploiting cooperative nonlinear interaction. Sci Adv 2022;8. https://doi.org/10.1126/sciadv.abp8483.

[11] Bloembergen N, Pound RV. Radiation damping in magnetic resonance experiments. Phys Ther Rev 1954;95:8–12. https://doi.org/10.1103/PhysRev.95.8.

[12] Chen HY, Lee Y, Bowen S, Hilty C. Spontaneous emission of NMR signals in hyperpolarized proton spin systems. J Magn Reson 2011;208:204–9. URL: https://www.ncbi.nlm.nih.gov/pubmed/21145766. https://doi.org/10.1016/j.jmr.2010.11.002.

[13] Weber EMM, Kurzbach D, Abergel D. A DNP-hyperpolarized solid-state water NMR MASER: observation and qualitative analysis. Phys Chem Chem Phys 2019;21:21278–86. URL, https://www.ncbi.nlm.nih.gov/pubmed/31549135. https://doi.org/10.1039/c9cp03334c.

[14] Chupp TE, Hoare RJ, Walsworth RL, Wu B. Spin-exchange-pumped 3He and 129Xe Zeeman masers. Phys Rev Lett 1994;72:2363–6. https://doi.org/10.1103/PhysRevLett.72.2363.

[15] Nelson C, Schmidt AB, Adelabu I, Nantogma S, Kiselev VG, Abdurraheem A, et al. Parahydrogen-induced carbon-13 radiofrequency amplification by stimulated emission of radiation. Angew Chem Int Ed Engl 2023;62:e202215678. URL, https://www.ncbi.nlm.nih.gov/pubmed/36437237. https://doi.org/10.1002/anie.202215678.

[16] Hope MA, Bjorgvinsdottir S, Grey CP, Emsley L. A magic angle spinning activated (17)O DNP Raser. J Phys Chem Lett 2021;12:345–9. URL: https://www.ncbi.nlm.nih.gov/pubmed/33355469. https://doi.org/10.1021/acs.jpclett.0c03457.

[17] Chikayama E, Ginthör SJ, Bechmann M, Müller N. Estimation of radiation damping rates using 133Cs, 7Li and 31P solution NMR spectroscopy and a theoretical NMR RASER model. Magnetochemistry 2023;9. https://doi.org/10.3390/magnetochemistry9100221.

[18] Bösiger P, Brun E, Meier D. Solid-state nuclear spin-flip maser pumped by dynamic nuclear polarization. Phys Rev Lett 1977;38:602–5. https://doi.org/10.1103/PhysRevLett.38.602.

[19] Adams RW, Aguilar JA, Atkinson KD, Cowley MJ, Elliott PIP, Duckett SB, et al. Reversible interactions with para-hydrogen enhance NMR sensitivity by polarization transfer. Science 2009;323:1708–11. https://doi.org/10.1126/science.1168877.

[20] Joalland B, Theis T, Appelt S, Chekmenev EY. Background-free proton NMR spectroscopy with radiofrequency amplification by stimulated emission radiation. Angew Chem Int Ed Engl 2021;60:26298–302. URL: https://www.ncbi.nlm.nih.gov/pubmed/34459080. https://doi.org/10.1002/anie.202108939.

[21] Suefke M, Lehmkuhl S, Liebisch A, Blümich B, Appelt S. Para-hydrogen raser delivers sub-millihertz resolution in nuclear magnetic resonance. Nat Phys 2017;13(6):568–72. URL: https://www.nature.com/articles/nphys4076. https://doi.org/10.1038/nphys4076.

[22] Fleischer S, Lehmkuhl S, Lohmann L, Appelt S. Approaching the ultimate limit in measurement precision with RASER NMR. Appl Magnet Resonan 2023;54:1241–70. https://doi.org/10.1007/s00723-023-01597-w.

[23] Appelt S, Lehmkuhl S, Fleischer S, Joalland B, Ariyasingha NM, Chekmenev EY, et al. SABRE and PHIP pumped RASER and the route to chaos. J Magn Reson 2021;

322:106815. URL, https://www.ncbi.nlm.nih.gov/pubmed/33423756. https://doi.org/10.1016/j.jmr.2020.106815.
[24] Lohmann L, Lehmkuhl S, Fleischer S, Rosen MS, Chekmenev EY, Theis T, et al. Exploring synchrony and chaos of parahydrogen-pumped two-compartment radio-frequency amplification by stimulated emission of radiation. Phys Rev A 2023;108. https://doi.org/10.1103/PhysRevA.108.022806.
[25] Yang J, Wang P, Korvink JG, J JB, Lehmkuhl S. The steady-state ALTADENA RASER generates continuous NMR signals. Chemphyschem 2023;24:e202300204. URL: https://www.ncbi.nlm.nih.gov/pubmed/37183171. https://doi.org/10.1002/cphc.202300204.
[26] Dong J, Fu J, He Z. A deep learning reconstruction framework for X-ray computed tomography with incomplete data. PloS One 2019;14:e0224426. URL, https://www.ncbi.nlm.nih.gov/pubmed/31675363. https://doi.org/10.1371/journal.pone.0224426.
[27] Fu L, De Man B. Deep learning tomographic reconstruction through hierarchical decomposition of domain transforms. Vis Comput Ind Biomed Art 2022;5:30. URL, https://www.ncbi.nlm.nih.gov/pubmed/36484980. https://doi.org/10.1186/s42492-022-00127-y.
[28] Jiang D, Dou W, Vosters L, Xu X, Sun Y, Tan T. Denoising of 3D magnetic resonance images with multi-channel residual learning of convolutional neural network. Jpn J Radiol 2018;36:566–74. URL, https://www.ncbi.nlm.nih.gov/pubmed/29982919. https://doi.org/10.1007/s11604-018-0758-8.
[29] Shen L, Zhao W, Xing L. Patient-specific reconstruction of volumetric computed tomography images from a single projection view via deep learning. Nature. Biomed Eng 2019;3:880–8. URL, https://www.nature.com/articles/s41551-019-0466-4. https://doi.org/10.1038/s41551-019-0466-4.
[30] LeCun Y, Bengio Y, Hinton G. Deep learning. Nature 2015;521:436–44. URL, https://www.ncbi.nlm.nih.gov/pubmed/26017442. https://doi.org/10.1038/nature14539.
[31] Appelt S, Kentner A, Lehmkuhl S, Blumich B. From LASER physics to the para-hydrogen pumped RASER. Prog Nucl Magn Reson Spectrosc 2019;114-115:1–32. URL: https://www.ncbi.nlm.nih.gov/pubmed/31779878. https://doi.org/10.1016/j.pnmrs.2019.05.003.
[32] Tobin J, Fong R, Ray A, Schneider J, Zaremba W, Abbeel P. Domain randomization for transferring deep neural networks from simulation to the real world. URL, https://ui.adsabs.harvard.edu/abs/2017arXiv170306907T.
[33] Knecht S, Blanchard JW, Barskiy D, Cavallari E, Dagys L, Van Dyke E, et al. Rapid hyperpolarization and purification of the metabolite fumarate in aqueous solution. Proc Natl Acad Sci U S A 2021;118. https://doi.org/10.1073/pnas.2025383118.
[34] Becker M, Arvidsson F, Bertilson J, Lehmkuhl S. Simulated 2D RASER MRI dataset for AI-driven artefact correction. 2024. https://doi.org/10.35097/1914.
[35] Ronneberger O, Fischer P, Brox T. U-net: Convolutional networks for biomedical image segmentation. In: Navab N, Hornegger J, Wells WM, Frangi AF, editors. Medical image computing and computer-assisted intervention – MICCAI 2015. Springer International Publishing; 2015. p. 234–41. https://doi.org/10.1007/978-3-319-24574-4{_}28.
[36] Wang Z, Bovik A, Sheikh H, Simoncelli E. Image quality assessment: from error visibility to structural similarity. IEEE Trans Image Process 2004;13(4):600–12. URL: http://ieeexplore.ieee.org/document/1284395/. https://doi.org/10.1109/TIP.2003.819861.
[37] Desvaux H. Non-linear liquid-state NMR. Prog Nucl Magn Reson Spectrosc 2013;70:50–71. URL, https://www.ncbi.nlm.nih.gov/pubmed/23540576. https://doi.org/10.1016/j.pnmrs.2012.11.001.
[38] Vlassenbroek A, Jeener J, Broekaert P. Radiation damping in high resolution liquid NMR: a simulation study. J Chem Phys 1995;103:5886–97. https://doi.org/10.1063/1.470468.
[39] Liaw R, Liang E, Nishihara R, Moritz P, Gonzalez JE, Stoica I. Tune: A research platform for distributed model selection and training. URL, https://ui.adsabs.harvard.edu/abs/2018arXiv180705118L.
[40] Zhang Y, Hu D, Hao S, Liu J, Quan G, Zhang Y, et al. DREAM-net: deep residual error iterative minimization network for sparse-view CT reconstruction. IEEE J Biomed Health Inform 2023;27(1):480–91. https://ieeexplore.ieee.org/document/9966660/. https://doi.org/10.1109/JBHI.2022.3225697.
[41] Arvidsson F, Bertilson J. Deep learning for the prediction of RASER-MRI profiles81; 2023. school = Linköping University, Media and Info.
[42] Paszke A, Gross S, Massa F, Lerer A, Bradbury J, Chanan G, et al. PyTorch: an imperative style, high-performance deep learning library. Adv Neural Inform Process Syst 2019;32:8024–35. URL, https://arxiv.org/pdf/1912.01703.pdf. http://arxiv.org/abs/1912.01703.
[43] Kingma DP, Ba J. Adam: A method for stochastic optimization. In: 3rd International conference on learning representations, ICLR 2015 - Conference track proceedings; 2014. URL, http://arxiv.org/abs/1412.6980.
[44] Yang J, Xin R, Lehmkuhl S, Korvink JG, Brandner JJ. Development of a fully automated workstation for conducting routine sabre hyperpolarization. Sci Rep 2024;14:21022.